Responses and Explanations on new the revision

(From the author of the manuscript egusphere-2025-5393, Qimeng Li)

18 March 2026

We sincerely thank the editor and the referees for their valuable and constructive comments on our manuscript. These comments have helped us improve the quality and clarity of the paper. We have carefully considered all the comments and revised the manuscript accordingly. Our detailed responses are provided below.

Response to Referee #1

Referee comment 1:

The authors calculate buoyancy acceleration (Eq. 9) using lidar-derived virtual potential temperature. While they state temperature uncertainties are <1 K and water vapor <0.5 g/kg (Table 1), they do not discuss how these errors propagate into the buoyancy and stability metrics. Given that the study relies heavily on small changes in stability to explain the "dome effect," a formal error propagation analysis is necessary to ensure the observed trends exceed the instrument's noise floor.

Author response:

Thank you very much for your insightful comments. We strongly agree with your suggestion and have added corresponding error propagation analysis for the calculation of buoyancy acceleration. Based on your suggestions, after careful consideration, we have made the following additions.

Changes in manuscript:

According to the theory of error propagation, the uncertainty of buoyancy acceleration can be expressed as:

$$\delta_B = \sqrt{\left(\frac{\partial B}{\partial \Gamma}\right)^2 \delta_\Gamma{}^2 + \left(\frac{\partial B}{\partial \Gamma}\right)^2 \delta_\theta{}^2} \quad , \qquad (10)$$

In the formula, $\Gamma = d\theta/dz_0$. The lidar system exhibits a high signal-to-noise ratio within the detection range below 4 km at night (2 km during daytime), and the temperature uncertainty is typically less than 0.5 K. Selecting typical boundary layer conditions with a virtual temperature of approximately 280K and a conservative uncertainty of 0.5 K, when the vertical resolution is 37.5m, the uncertainty of the temperature gradient obtained is approximately 0.019 K m^{-1}, and the uncertainty of the buoyancy acceleration is calculated to be approximately 0.025 m s^{-2}. This value represents the worst-case scenario assuming completely uncorrelated errors. Lidar temperature errors exhibit strong vertical correlation, and buoyancy is essentially derived from vertical gradients. Therefore, the effective uncertainty in buoyancy is substantially smaller. Although this uncertainty may affect very weak buoyancy signals near neutral conditions, the identification of stable layers and strong inversions is robust. (In page 9, lines 194-203)

Referee comment 2:

The manuscript frequently employs strong causal language that may not be fully supported by the observational evidence. For instance, the authors state that clouds and virga "drove" suppressing

radiative heating and the rapid increase in $PM_{2.5}$. While the temporal correlation is evident, the study does not sufficiently account for confounding factors such as variations in local primary emissions or regional advection during these specific windows. Furthermore, the discussion of the "stove effect" is somewhat contradictory; it is described as "favoring" pollution alleviation, yet the authors simultaneously conclude that surface-based TIs rendered this effect "negligible". A more rigorous analysis, perhaps involving a mass-balance approach or sensitivity tests, is required to disentangle these competing meteorological and chemical mechanisms.

Author response:

We appreciate your constructive comments. Following your suggestions, we carefully reviewed the manuscript and revised statements where the supporting evidence was insufficient.

For the virga event observed during the night of 28 December, we examined 48-hour backward air-mass trajectories at multiple altitudes (0.5, 1.5, and 3.0 km). The results indicate that airflows at approximately 0.5 km and 1.5 km were predominantly advected from southern regions toward the observation site, with relatively short transport pathways and limited residence over major upwind pollution source regions. In contrast, air masses at 3.0 km originated mainly from the west to northwest and were less directly coupled to the near-surface aerosol layer. These trajectory characteristics suggest that large-scale regional transport was unlikely to be the dominant contributor to near-surface aerosol loading during this period. Meanwhile, strict emission control measures were implemented in Xi'an, including traffic restrictions and industrial emission limits, which likely reduced local primary emissions.

Under these conditions, the observed haze development is more plausibly associated with unfavorable boundary-layer dynamics, particularly the presence of a stable temperature inversion and weak near-surface ventilation, which suppressed vertical mixing and promoted pollutant accumulation. This interpretation is consistent with the concurrent stagnation of low-level air masses and the nighttime radiative cooling environment during the virga event.

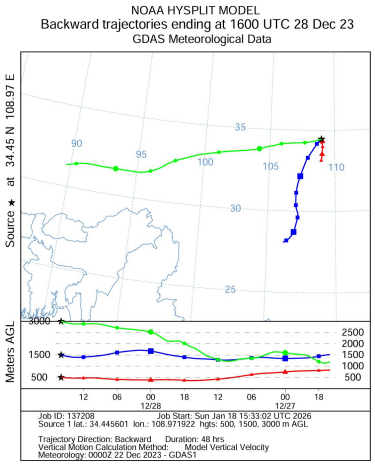

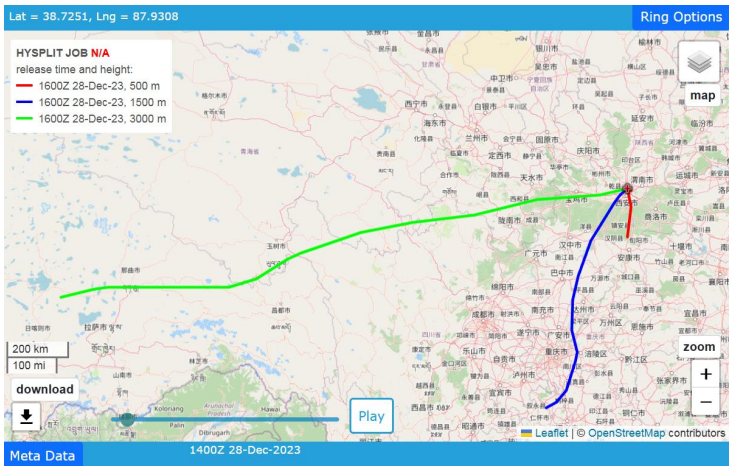

We apologize for the previous lack of clarity regarding the relationship between the "stove effect" and the surface-based TI, and have made corresponding revisions in the manuscript (In page 18, lines 345-347. "However, the radiosonde temperature profile on the morning of 24 December (Fig. 6f) indicates the presence of a near-surface inversion, which may delay surface warming and the development of turbulence in the lower atmosphere and could partly explain the relatively small

variation in surface $PM_{2.5}$ concentrations."). We would like to clarify that, although the stove effect within the lower layer favors warming and may enhance upward turbulent mixing, the surface inversion formed by nocturnal radiative cooling may delay the development of near-surface turbulence.

Changes in manuscript:

To assess the role of large-scale transport in the development of the pollution episode, 48 h backward air-mass trajectories at multiple altitudes (0.5, 1.5, and 3.0 km) were analyzed for 28 December, which was characterized by severe pollution. The results indicate that airflows at approximately 0.5 km and 1.5 km were predominantly advected from southern regions toward the observation site, with relatively short transport pathways and limited residence time over major upwind pollution source areas. In contrast, air masses at 3.0 km mainly originated from the west to northwest and exhibited weak coupling with the near-surface aerosol layer. Consequently, large-scale regional transport is unlikely to be the dominant factor governing the near-surface aerosol loading during this period. Moreover, strict emission control measures were implemented in Xi'an, including traffic restrictions and constraints on industrial emissions, which may have further reduced local primary emissions. (In page 12, lines 263-271)

Referee comment 3:

The study places heavy emphasis on the "stove effect" and "surface-based temperature inversions (TIs)," both of which occur in the lowest few hundred meters of the atmosphere. However, most Raman-Mie lidar systems suffer from a "blind zone" or "overlap effect" in the first 200–500 meters. While the authors mention a "geometric overlap factor correction" (referencing Li et al., 2025), they do not show the overlap function or discuss the minimum height at which the temperature and humidity retrievals become stable. What is the full-overlap height of the system? If the overlap correction is significant below 500m, how can the authors ensure that the "stove effect" observations (often very close to the surface) are not artifacts of the correction algorithm?

Author response:

Thank you very much for the reviewer's insightful comments. As pointed out, the stove effect and surface-based temperature inversions predominantly occur within the lowest few hundred meters of the atmosphere. The complete overlap blind zone of the lidar system developed in this study is approximately 120 m; therefore, the minimum theoretical detection height of the system is about 120 m.

Although inconsistency between the two rotational Raman channels may exist, the relative relationship between the channels is generally stable and primarily determined by the system hardware configuration. For the present system, the height range affected by incomplete overlap between the two rotational Raman channels extends up to approximately 600 m. To address this issue, corresponding correction procedures have been applied to ensure reliable temperature retrievals within the incomplete-overlap region. This correction approach has been previously published in Acta Optica Sinica (DOI: 10.3788/AOS241641, Li, Q., Di, H., Chen, N., Cheng, X., Yang, J., Bai, S., Dou, J., Yan, Q., Li, S., Xin, W., Wang, Y., and Hua, D.: Detection and correction techniques of atmospheric temperature profiles within the boundary layer during haze days, Acta Op. Sin., 45(3): 0312003, https://doi.org/10.3788/AOS241641, 2025).

We apologize that the technical methodology was not described with sufficient clarity in the

original manuscript. In response to the reviewer's comments, we have now provided a more detailed explanation of the relevant techniques and corrections. Specifically, a description of the system pure blind-zone height has been added (In page 3, line 75. "The complete overlap blind zone of the system is approximately 120 m"), Fig. 1 in the original manuscript (now Fig. 2 in the revised version) illustrating the temperature retrieval process has been revised, and additional details on near-surface atmospheric temperature measurements have been added. Further descriptions are provided in Response to Comment 7.

Changes in manuscript: (In pages 7-8, lines 168-181)

The atmospheric temperature correction technique is based on establishing a linear relationship between the backscatter ratio and the elastic-scattering crosstalk ratio, which allows the rotational Raman ratio to be corrected using the measured backscatter ratio. Figure 2 illustrates the temperature retrieval process based on this algorithm. First, a high-altitude region unaffected by the geometric overlap factor is selected, and radiosonde temperature profiles are used for system calibration. Under clear-sky and dry near-surface conditions, the theoretical rotational Raman ratio is derived from radiosonde data (black dash–dotted line in Fig. 2a). By comparing it with the measured Raman ratio (blue solid line in Fig. 2a), the geometric overlap factor is obtained (red solid line in Fig. 2b), enabling overlap correction. Next, the theoretical Raman ratio under strong elastic-scattering conditions is derived from radiosonde data (black dash–dotted line in Fig. 2d). The measured Raman ratio (black solid line in Fig. 2d) is then used to calculate the elastic-scattering crosstalk ratio. A linear regression between the backscatter ratio and the crosstalk ratio is performed to determine the system calibration constant (Fig. 2e). Using this constant together with the measured backscatter ratio, the rotational Raman ratio is corrected, enabling retrieval of the atmospheric temperature profile within the elastic-scattering region (Fig. 2f). A linear regression between the corrected lidar temperature and the radiosonde temperature yields a coefficient of determination (R^2) of approximately 0.8 (Fig. 2g), indicating good agreement between the two measurements. A detailed description of the algorithm can be found in Li et al. (2025).

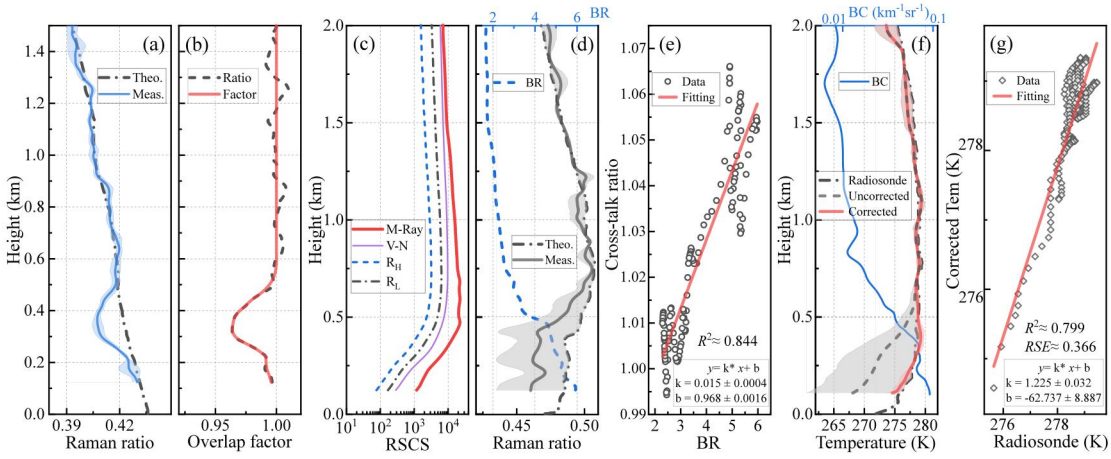

Figure 2. Atmospheric temperature correction. (a) Measured (blue solid) and theoretical (black dash–dotted) rotational Raman ratios. (b) Overlap-related quantities, including the measured ratio (black dashed) and the overlap function (red solid). (c) Range-square-corrected signals from the elastic (Mie–Rayleigh; thick red solid), nitrogen vibrational Raman (thin purple solid), and high- and low-quantum-number rotational Raman (black dash–dotted and blue dashed) channels. (d) Backscatter ratio (blue dash–dotted) and rotational Raman ratios (measured ratio, black solid; theoretical ratio, black dash–dotted). (e) Linear regression between the backscatter ratio (BR) and the cross-talk ratio. (f) Backscatter coefficient (BC) and temperature profiles derived from lidar measurements and radiosonde observations. The black dash–dotted line denotes the radiosonde temperature, while the red solid and blue dashed lines represent the corrected and uncorrected lidar temperature profiles, respectively.

Shaded areas indicate the corresponding uncertainties. (g) Linear regression between radiosonde and lidar temperatures.

Referee comment 4:

Does the system provide depolarization measurements? If so, these should be included to confirm the presence of virga and characterize the aerosol type. If not, the authors must clarify how they distinguish between high-extinction "heavy haze" and "cloud base" or "virga" using only backscatter and Raman signals, as these features can look very similar in elastic channels.

Author response:

We sincerely thank you for your valuable suggestion. The depolarization ratio is indeed an important parameter for distinguishing cloud base, virga, and haze, and it also provides useful information for aerosol type characterization. Our lidar system is capable of measuring the depolarization ratio. However, due to instrumental and data availability limitations, part of the depolarization channel data during the study period was missing, and therefore these results were not included in the original manuscript. Following your suggestion, we processed the available depolarization ratio data for the virga event on 1 January 2024. The results show that within the virga region, the depolarization ratio decreases significantly with increasing range-square-corrected signal (RSCS). In addition, the depolarization ratio is markedly reduced above the cloud-base boundary, indicating that the cloud base exhibits typical liquid-water cloud characteristics. In this study, virga identification is primarily based on the combined Mie–Rayleigh backscatter signals at 1064 nm and 355 nm. It is acknowledged that distinguishing the transition region between haze and cloud using a single vertical profile may involve certain uncertainties. However, continuous lidar observations provide highly correlated features in both the temporal and vertical dimensions, which facilitates a more reliable identification of heavy haze, cloud layers, and virga structures. In addition, to further validate this conclusion, we also retrieved corresponding millimeter-wave radar data for the same periods. As shown in the figure, the vertical velocity and echo reflectivity provide additional evidence supporting the occurrence of the virga events.

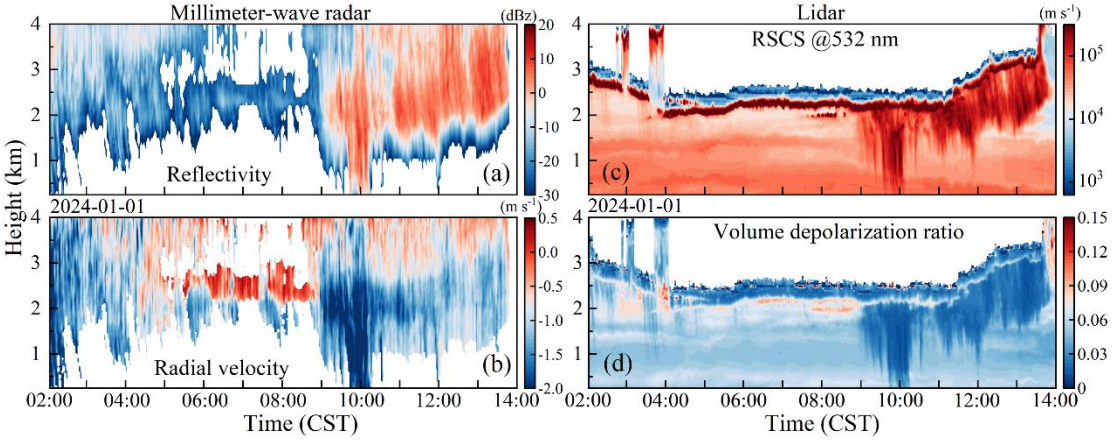

Similar virga phenomena have also been reported in previous lidar-based studies. For example, Yi et al. (Yi, Y., Yi, F., Liu, F., Zhang, Y., Yu, C., and He, Y.: Microphysical process of precipitating hydrometeors from warm-front mid-level stratiform clouds revealed by ground-based lidar observations, Atmos. Chem. Phys., 21, 17649–17664, https://doi.org/10.5194/acp-21-17649-2021, 2021.) revealed the microphysical processes of precipitating hydrometeors in warm-front

mid-level stratiform clouds using ground-based lidar observations and documented comparable virga-like structures during the precipitation evolution, , as shown in the corresponding figure.

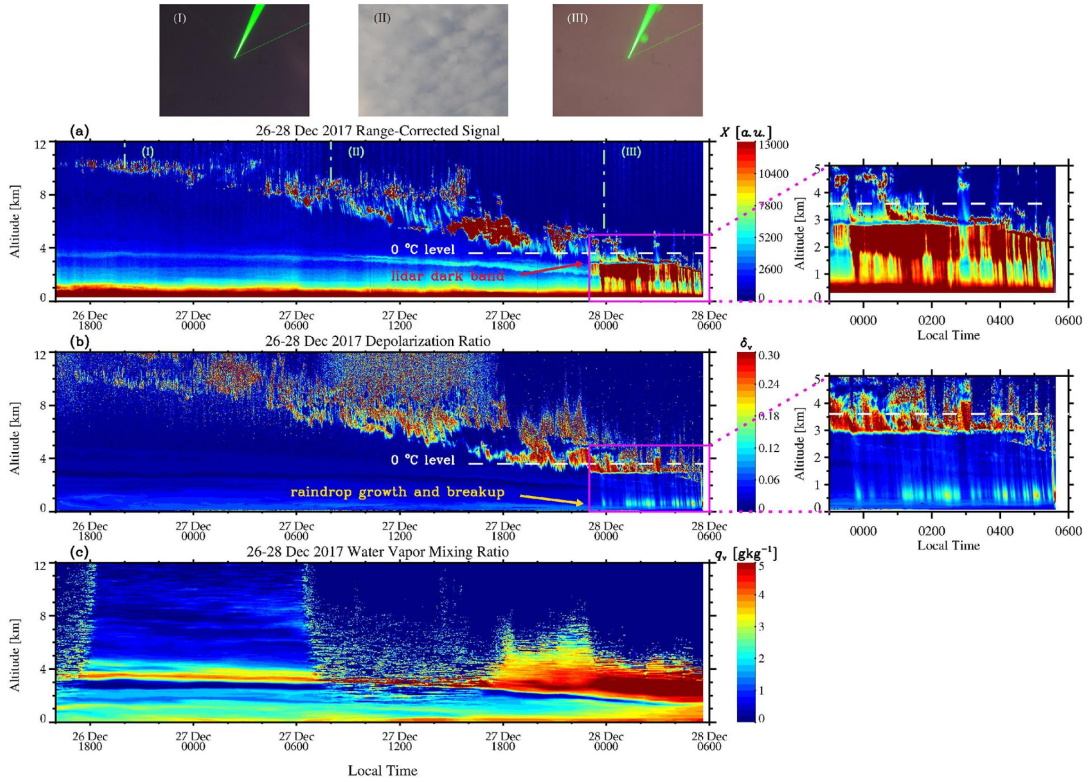

Figure 2. Time–height contour plots (1 min and 30 m resolution) of the **(a)** range-corrected signal X, **(b)** volume depolarization ratio δ_V measured by a 355 nm polarization lidar and **(c)** water vapor mixing ratio q_V measured by a water vapor Raman lidar on 26–28 December 2017, which exhibited the passage of a warm front and the resulting hours-long light rain. A sliding average of 60 min was applied to the Raman lidar data. The precipitation streaks surrounded by magenta lines are zoomed in to show their details. Shown on the top of the figure are the corresponding photographs of the sky taken by a ground-based camera at our lidar site, with the third photograph exhibiting the sky illuminated by a 532 nm laser beam during the onset of rainfall.

Changes in manuscript:

As shown in Fig. 6a, three distinct cloud events occurred in the upper atmosphere during the pollution episode, specifically on 22–23 December 2023, 28–29 December 2023, and 31 December 2023–1 January 2024. All three events were observed to coincide with reductions in surface radiation. The second and third cloud events were accompanied by virga, during which increased near-surface relative humidity was observed, temporally coinciding with periods of elevated surface pollution. The continuous vertical profile of the lidar Mie–Rayleigh backscatter signal served as the primary basis for the preliminary identification of cloud layers and virga, which could be further corroborated by depolarization ratio measurements or radial velocity observations from millimeter-wave radar (Yi et al., 2021; Zou et al., 2024; Jimenez et al., 2025). (In pages 13-14, lines 282-288)

Two additional references have been added accordingly.

Jimenez, C., Ansmann, A., Ohneiser, K., Griesche, H., Engelmann, R., Radenz, M., Hofer, J., Althausen, D., Knopf, D. A., Dahlke, S., Bühl, J., Baars, H., Seifert, P., and Wandinger, U.: MOSAiC studies of long-lasting mixed-phase cloud events and analysis of the liquid-phase properties of Arctic clouds, Atmos. Chem. Phys., 25, 12955–12981, https://doi.org/10.5194/acp-25-12955-2025, 2025. (In page 29, lines 566-568)

Zou, W., Yin, Z., Dai, Y., Chen, Bu, Z., Li, S., He, Y., Hu, X., Müller, D., Lu, T., Dong, X., and Wang, X.: Robust lidar-radar composite cloud boundary detection method with rainfall pixels removal, IEEE Trans. Geosci. Remote Sen., 62, https://doi.org/10.1109/TGRS.2024.3476127, 2024. (In page 31, lines

635-637)

Referee comment 5:

The paper identifies three specific "dome-type TIs". The criteria for classifying an inversion as "dome-type" versus a standard elevated inversion should be more explicitly defined. Is this based purely on the geometric shape of the PM5 stratification, or on a specific threshold of radiative heating/cooling rates?

Author response:

We thank you for your valuable suggestion. The "dome-type TIs" mentioned in the manuscript is primarily defined based on the geometric structure of the observed temperature distribution and the $PM_{2.5}$ stratification. Strictly speaking, it can be classified as a persistent elevated inversion with a dome-like structure, which notably suppresses turbulent motions in the boundary layer. Following your suggestion, we have added a description in the revised manuscript clarifying the basis for defining the dome-shaped inversion.

Changes in manuscript:

Furthermore, three persistent “capping inversion” layers with a dome-like structure were observed during the pollution development stage and are hereafter referred to as dome-type TIs, as indicated by the green dashed regions in Fig. 6d. The identification of dome-type TIs relies primarily on the geometric structure of the vertical temperature profiles and the corresponding aerosol-layer stratification. A comparison with Fig. 8o shows that the daily mean surface $PM_{2.5}$ concentrations tend to increase as the dome height decreases and decrease as the dome height increases. Although the dome height on 28 December was relatively high, severe pollution was still observed, suggesting that factors such as aerosol hygroscopic growth under high relative humidity may have contributed. (In page 19, lines 360-366)

Referee comment 6:

To truly claim an "Aerosol-Radiation-Boundary Layer" feedback, could the authors provide a simple estimation of the heating rate induced by the aerosol layer? This would support the "dome effect" hypothesis by showing that the aerosol-induced warming at the top of the layer is sufficient to maintain the observed temperature inversion.

Author response:

We thank the reviewer for this constructive comment. We have added a simple estimation of the aerosol-induced heating rate in the revised manuscript. The heating rate is diagnostically estimated using a simplified shortwave heating formulation based on the vertical gradient of the net radiative flux. The results indicate that the heating rate is noticeably enhanced within the aerosol-stratified region, especially near the top of the layer. Although this estimation is simplified, the enhanced aerosol-induced warming is consistent with the presence and persistence of the observed temperature inversion.

Changes in manuscript:

(In pages 19-21, lines 367-388)

The hourly evolution of the aerosol vertical structure, atmospheric temperature, and buoyancy acceleration on 25 December is shown in Fig. 10a. Figure 10b presents the variations in temperature tendency, temperature gradient, and TI depth of the elevated TI layer. Figure 10c

shows the aerosol heating rate, which is approximately estimated using a simplified shortwave heating formulation in the vertical direction ($Q = 1/(\rho c_p)\cdot dF/dz$), where ρ and c_p denote the air density and the specific heat capacity of air, respectively, and F represents the net radiative flux. The lidar ratio at 355 nm ($S=\alpha/\beta$) is shown in Fig. 10d.

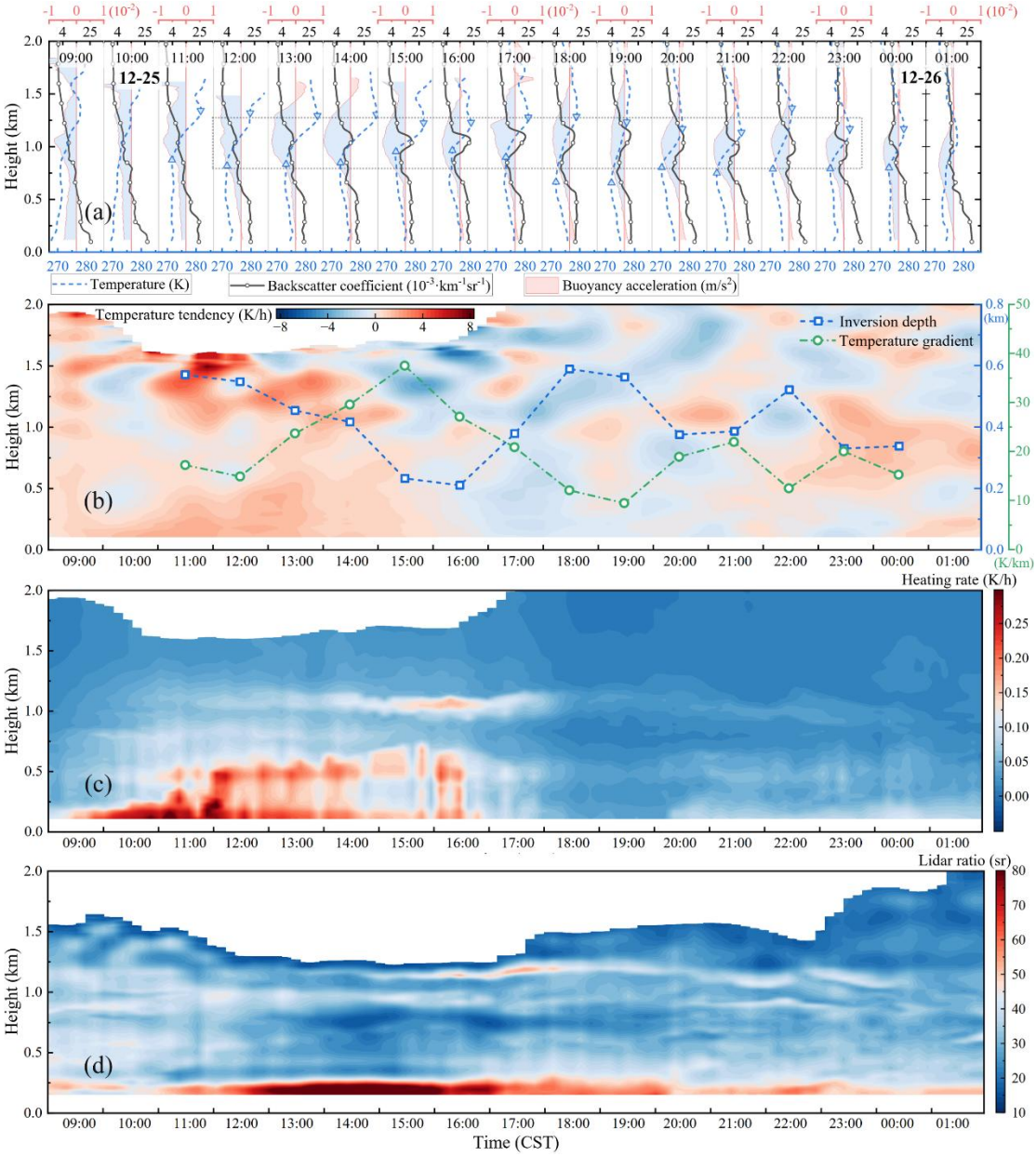

Figure 10. Evolution of the vertical structure and atmospheric buoyancy on 25 December. Panels (a)–(d) show the aerosol and temperature structure, buoyancy acceleration, aerosol heating rate, and lidar ratio (355 nm), respectively. In panel (a), the black line with circle markers represents the aerosol backscatter coefficient, and the blue dashed line denotes the temperature profile. Shading indicates buoyancy acceleration, with blue (red) corresponding to negative (positive) values and downward (upward) buoyant motion. Upward- and downward-pointing triangles indicate the TI layer. In panel (b), the green dotted line shows the temperature gradient, while the blue dash–dotted line with square markers represents the TI depth.

Under the combined influence of the elevated TI and weak surface convection, a dome-like stratified structure began to develop near the UABL. As illustrated in Fig. 10b, after 10:00 local standard time (LST), the temperature tendency around 1.2 km increases significantly and is markedly higher than that in the lower layers, whereas the aerosol heating rate in Fig. 10c remains relatively weak. Backward air-mass trajectory analysis shows that the airflow at approximately 1.5 km is advected from southern regions toward the observation site, indicating a northward transport

of warm air. Consequently, horizontal advection may play an important role in the pronounced warming near the upper boundary layer (UABL). Under the combined influence of advective warming and aerosol radiative heating (in Figs. 10c–d), the elevated TI appears to be further intensified. This process is likely to suppress the upward transport of turbulence and induce local aerosol subsidence. Meanwhile, surface warming may enhance buoyancy in the lower atmosphere (in Figs. 10c–d), promoting turbulent uplift of near-surface aerosols. However, the heating rate near the surface remains relatively weak.

As a pronounced stratification develops near the UABL, the heating rate within the aerosol-stratified layer increases substantially, while the warming rate in the lower layer tends to decrease. This reduction may be partly attributed to the attenuation of downward radiative fluxes by the stratified aerosol layer, which could constrain surface warming. Given the mid-latitude location of the study region, the limited duration of daytime solar radiation may have been insufficient to sustain continuous surface heating. Consequently, subsidence within the upper aerosol layer likely became the dominant mechanism regulating vertical aerosol mixing during this period. These interpretations are based on observational consistency and are subject to uncertainties associated with the simplified heating rate estimation. (In pages 19-21, lines 367-388)

Referee comment 7:

The Raman ratio correction and geometric overlap factor correction are central to the paper's novelty. While the authors refer to Li et al. (2025) for details, a brief but more comprehensive summary of how the "theoretical rotational Raman ratio" is derived from radiosondes and applied to the "haze layer" retrievals would improve the manuscript's readability and transparency.

Author response:

Thank you for your comment. In response, we have added a detailed description of the atmospheric temperature correction procedure and revised Fig. 1 and its caption to clarify the retrieval steps and the physical meaning of each panel.

Specifically, the core of the atmospheric temperature correction method is to establish a linear functional relationship between the backscatter ratio and the elastic scattering crosstalk ratio, which is then used to correct the rotational Raman ratio. A high-altitude region unaffected by the geometric overlap factor is first selected and combined with radiosonde temperature profiles for system calibration. Under clear-sky and dry near-surface conditions, the theoretical rotational Raman ratio is derived from radiosonde data and compared with the measured ratio to obtain the geometric overlap factor correction. Subsequently, under strong elastic scattering conditions, the elastic scattering crosstalk ratio is determined using the measured and theoretical Raman ratios. A linear regression analysis between the backscatter ratio and the elastic scattering crosstalk ratio is then performed to derive the system calibration constant, which is finally applied to correct the rotational Raman ratio and retrieve the true atmospheric temperature profile in the elastic scattering region.

In addition, Fig. 1 and its caption have been carefully revised to explicitly describe each panel, including the measured and theoretical Raman ratios, the overlap-related quantities, the range-squared-corrected signals of different channels, the backscatter ratio, the regression analysis, and the resulting temperature profiles with and without correction. These revisions are intended to improve the clarity and reproducibility of the retrieval algorithm. Detailed descriptions of the

algorithm and procedures are provided in Li et al. (2025, DOI: 10.3788/AOS241641).

Changes in manuscript:

The relevant revisions in the manuscript can be found in the response to Comment 3.

Referee comment 8:

The study is conducted in Xi'an, located in the Guanzhong Plain, a narrow basin bordered by the Qinling Mountains to the south. Local phenomena like "dome effects" and "stove effects" are driven by urban-scale (1–5 km) or valley-scale thermodynamics. A 31 km grid cell is far too coarse to "see" the specific vertical air currents or temperature variations created by the interaction between the city's heat and the nearby mountain slopes. The authors explicitly state that they derive vertical velocity from the "vertical pressure tendency provided by ERA5". Vertical velocity is one of the most difficult variables for reanalysis models to get right at a local level. In a complex basin, the actual vertical motion measured by the lidar (which has a resolution of 3.75 m) might be completely different from the average vertical motion of a 31 km x 31 km block in ERA5. Using a coarse, model-averaged vertical velocity to explain fine-scale aerosol stratification observed by a lidar can be misleading. Specifically, how do the authors justify using a 31 km grid-averaged vertical velocity to interpret aerosol stratification changes observed at a local station? A discussion on the representativeness of ERA5 vertical motion for these specific local events is required.

Author response:

We thank the reviewer for raising this important and fundamental concern. We fully agree that vertical velocity is one of the most uncertain variables in reanalysis products, especially at local scales and in complex terrain such as the Guanzhong Basin. In the revised manuscript, we clarify that ERA5-derived vertical velocity is not used to quantitatively interpret the fine-scale aerosol stratification observed by the lidar. Instead, it is employed solely to characterize the large-scale synoptic background, such as periods of weak subsidence or ascent that provide a favorable or unfavorable environment for boundary-layer development. While ERA5 vertical velocity cannot represent local-scale updrafts or downdrafts within the urban boundary layer, it can still indicate whether the regional atmosphere is under weak large-scale subsidence or ascent. Such background conditions can modulate the persistence and vertical confinement of aerosols, without directly determining their fine vertical structure. We therefore avoid any one-to-one interpretation between ERA5 vertical velocity and the lidar-observed aerosol layers. The lidar observations remain the primary and direct diagnostic of local aerosol stratification and boundary-layer thermodynamic structure.

Changes in manuscript:

Figure 7 presents the continuous distributions of potential temperature, buoyancy acceleration, and vertical velocity. The vertical velocity used in this study was derived from the vertical pressure tendency provided by ERA5. It is noteworthy that ERA5-derived vertical velocity is not used to quantitatively interpret the fine-scale aerosol stratification observed by the lidar. Instead, it is employed solely to characterize the large-scale synoptic background, such as periods of weak subsidence or ascent that provide a favorable or unfavorable environment for boundary-layer development. (In page 14, lines 296-300)

Referee comment 9:

Are UABL and PBLH herein different? Kindly ensure if "UABL" (Upper Boundary of Aerosol Layer) is defined at its first mention in the main text and used consistently. Currently, the text occasionally switches between discussing "PBLH" and "UABL".

Author response:

Thank you for pointing out the critical issue, and sorry for this misstatement. The main research object of this article is the upper boundary of aerosol layer (UABL). According to your suggestions, we have replaced the statement about "PBLH" in the article with "the height of UABL" to ensure the consistency of the research object.

Changes in manuscript:

Furthermore, the UABL height showed a strong positive correlation with the top height of the TI layer ($R^2 \approx 0.57$). For the TI layer near the UABL, the temperature gradient exhibited a piecewise negative correlation with $PM_{2.5}$ concentrations. (In page 28, lines 515-517)

Response to Referee #2

Referee comment 1:

The authors use multiple datasets and discuss different variables, in the manuscript some of the instrumentation, methodology and uncertainties are described, but there is a lack of information on others, like $PM_{2.5}$, PM_{10} and meteorological and radiometric measurements at the surface level. This is worthy information to be included, bearing in mind some of the correlation analyses included in the manuscript.

Author response:

We thank the reviewer for pointing out this important issue. We agree that, given the correlation analyses presented in the manuscript, a comprehensive description of the surface measurements is essential.

Changes in manuscript:

PM_{10} and $PM_{2.5}$ concentrations were measured using β-ray absorption particulate matter monitors (LGH-01B and LGH-01E). Both instruments operate over a concentration range of 0−1000 μg m^{-3}, with a minimum sampling interval of 30 min and a sampling flow rate of 16.7 L min^{-1}. The lower detection limit is < 2 μg m^{-3}, and the flow stability is within 2 %. Surface meteorological variables were obtained from an automatic weather station (DZZ5). Atmospheric pressure is measured over a range of 500–1100 hPa with a resolution of 0.1 hPa and a maximum permissible error of ±0.3 hPa. Air temperature is measured over a range of −50 to 50 °C, with a resolution of 0.1 °C and a maximum permissible error of ±0.2 °C. Relative humidity is measured over 5–100 %, with a resolution of 1 %, and maximum permissible errors of ±3 % for RH ≤ 80 % and ±5 % for RH > 80 %.Surface solar irradiance was measured using a TBQ-2-UMB pyranometer, which has a spectral response range of 0.3–3 μm and a measurement range of 0–2000 W m^{-2}. The hourly measurement uncertainty is approximately 8 %. (In page 4, lines 92-100)

Referee comment 2:

Section 2.2 must be improved with the inclusion of some graphical information on the study area.

Author response:

Thank you very much for this valuable suggestion. We fully agree with the reviewer's comment and have added a map of the study area in Section 2.2. The geographical information of the study area is now shown in Fig. 1.

Changes in manuscript:

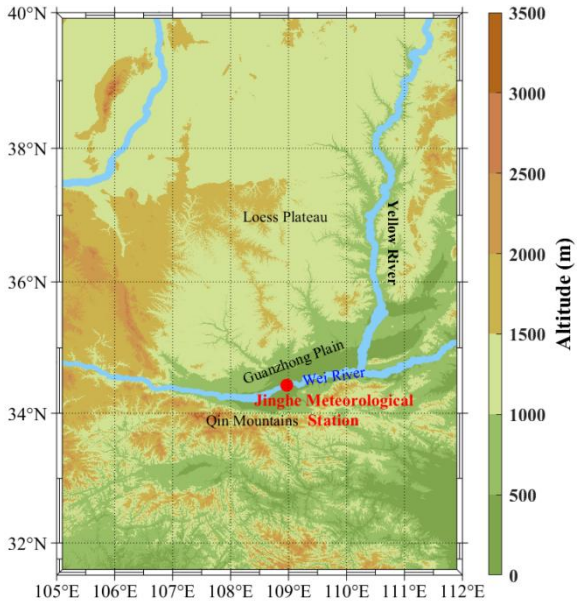

Figure 1. Geographical coverage around observation site (31°30′–40°N, 105°–112°E). The red dot indicates the location of the Jinghe National Meteorological Station in Xi'an (34°26′N, 108°58′E).

(In page 6, lines 131-132)

Referee comment 3:

Given the relevance of the temperature and relative humidity profiling and the accessibility of the reference Li et al. 2025, additional details on the associated methodology must be included in the manuscript for helping the reader understand better the pros and cons of these retrievals. I realized that the authors provided yet an answer to this question through the answer they gave to the Reviewer#1 review. But concerning the new figure 1, and the explanation offered in the answer to the Reviewer #1, I do not understand the small size of the shaded area associated to the corrected temperature profile in red, having in mind the uncertainty associated to the cross talk correction method, evidenced in the new figure 1g, where it is necessary to include information on the regression coefficient and the standard error of the modelled cross-talk.

Author response:

We thank the reviewer for this detailed and technically important comment. Because the absolute error of the uncorrected temperature is relatively large, displaying the full absolute error of the uncorrected temperature (grey shading) would reduce the visibility of the corrected temperature absolute error (red shading). We fully agree with your suggestion and have therefore added a linear regression analysis between the cross-talk–corrected temperature profile and the radiosonde temperature profile in Fig. 1 in the original manuscript (now Fig. 2 in the revised version). The

regression coefficients and standard deviation information are also provided to improve transparency. The cross-talk regression yielded $R^2 \approx 0.799$ (n=372, ≤1.5 km), with a residual standard error of 0.366 K.

Changes in manuscript: (In pages 7-8, lines 168-182)

The atmospheric temperature correction technique is based on establishing a linear relationship between the backscatter ratio and the elastic-scattering crosstalk ratio, which allows the rotational Raman ratio to be corrected using the measured backscatter ratio. Figure 2 illustrates the temperature retrieval process based on this algorithm. First, a high-altitude region unaffected by the geometric overlap factor is selected, and radiosonde temperature profiles are used for system calibration. Under clear-sky and dry near-surface conditions, the theoretical rotational Raman ratio is derived from radiosonde data (black dash–dotted line in Fig. 2a). By comparing it with the measured Raman ratio (blue solid line in Fig. 2a), the geometric overlap factor is obtained (red solid line in Fig. 2b), enabling overlap correction. Next, the theoretical Raman ratio under strong elastic-scattering conditions is derived from radiosonde data (black dash–dotted line in Fig. 2d). The measured Raman ratio (black solid line in Fig. 2d) is then used to calculate the elastic-scattering crosstalk ratio. A linear regression between the backscatter ratio and the crosstalk ratio is performed to determine the system calibration constant (Fig. 2e). Using this constant together with the measured backscatter ratio, the rotational Raman ratio is corrected, enabling retrieval of the atmospheric temperature profile within the elastic-scattering region (Fig. 2f). A linear regression between the corrected lidar temperature and the radiosonde temperature yields a coefficient of determination (R^2) of approximately 0.8 (Fig. 2g), indicating good agreement between the two measurements. A detailed description of the algorithm can be found in Li et al. (2025).

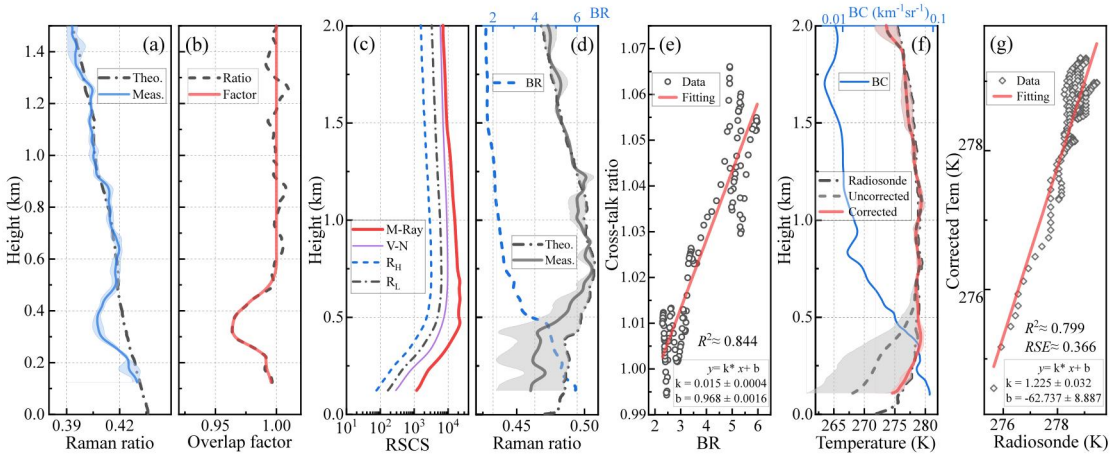

Figure 2. Atmospheric temperature correction. (a) Measured (blue solid) and theoretical (black dash–dotted) rotational Raman ratios. (b) Overlap-related quantities, including the measured ratio (black dashed) and the overlap function (red solid). (c) Range-square-corrected signals from the elastic (Mie–Rayleigh; thick red solid), nitrogen vibrational Raman (thin purple solid), and high- and low-quantum-number rotational Raman (black dash–dotted and blue dashed) channels. (d) Backscatter ratio (blue dash–dotted) and rotational Raman ratios (measured ratio, black solid; theoretical ratio, black dash–dotted). (e) Linear regression between the backscatter ratio (BR) and the cross-talk ratio. (f) Backscatter coefficient (BC) and temperature profiles derived from lidar measurements and radiosonde observations. The black dash–dotted line denotes the radiosonde temperature, while the red solid and blue dashed lines represent the corrected and uncorrected lidar temperature profiles, respectively. Shaded areas indicate the corresponding uncertainties. (g) Linear regression between radiosonde and lidar temperatures.

Referee comment 4:

The discussion on figure 7 is not easy to follow, the redesign of this figure could help to solve this

problem. In general, the sizes of figures could be larger to clearly detect the significant features of the situation. Likely shortening the number of time slots presented and improving the visibility of the most relevant periods. Identifications of the upper aerosol layer and the top of the TI in the profiles of figure 7 could improve the discussion.

Author response:

We thank the reviewer for the constructive comments. Figure 7 in the original manuscript (now Figure 8 in the revised version) is primarily intended to illustrate the day-to-day evolution of the vertical structures of aerosols and temperature during the pollution development stage. To facilitate comparison between the vertical structures of aerosols and temperature, we have redesigned Fig. 7 (now Figure 8 in the revised version) following your suggestion. Specifically, the font size of the text and numerical labels in the figure has been increased to improve the visualization of the key information.In addition, we focus on the vertical structure distributions in the morning and evening to highlight the characteristic features during these important periods more clearly. The upper boundary of the aerosol layer and the top of the temperature inversion have been specifically marked in the figure.

We carefully checked the entire manuscript and found that the font size in Fig. 2 (now Figure 3 in the revised version) also required adjustment. Therefore, the figure has been redrawn to improve its visual clarity, as shown below.

Changes in manuscript:

(1) (In page 17, lines 331-332)

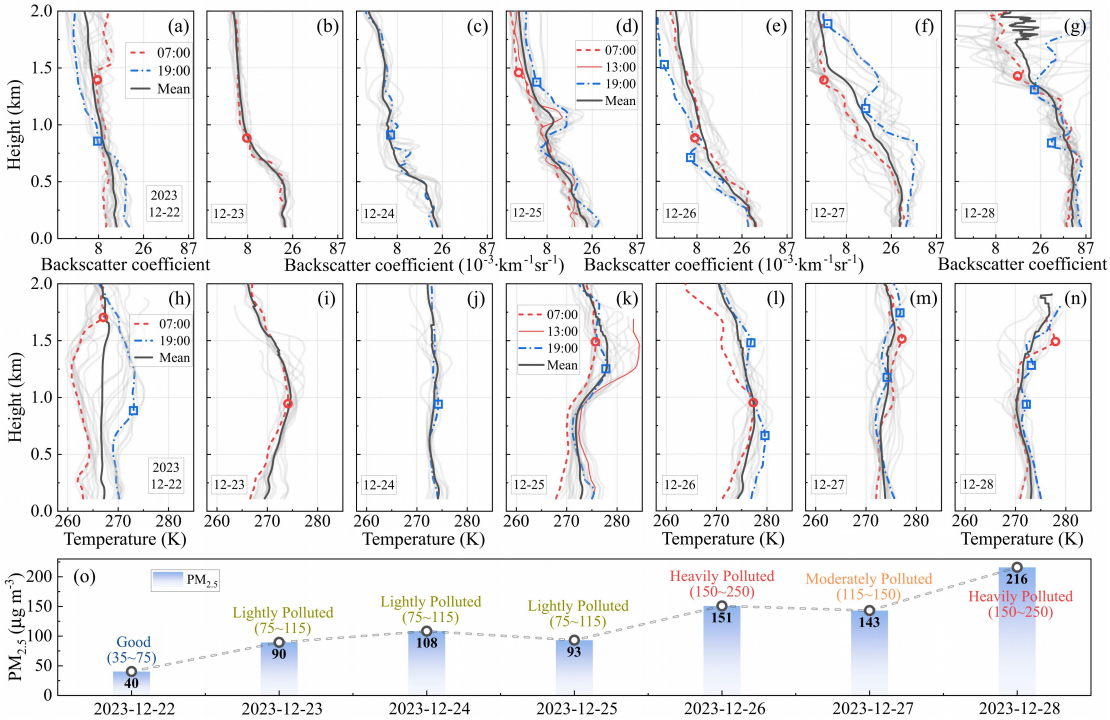

Figure 8. Vertical profiles of aerosol backscatter coefficient and temperature from 22 to 28 December. Panels (a)–(g) show the aerosol backscatter coefficient profiles. The red dashed and blue dash–dotted lines denote the profiles at 07:00 and 19:00, respectively. The black solid line represents the daily mean profile, while the grey solid lines indicate hourly profiles. Red circles and blue squares mark the upper boundary of the aerosol layer in the morning and evening, respectively. Panels (h)–(n) show the temperature profiles with the same plotting conventions. Red circles and blue squares indicate the top heights of the TI in the morning and evening, respectively. Panel (o) shows the daily mean $PM_{2.5}$ concentrations.

(2) (In page 10, lines 223-224)

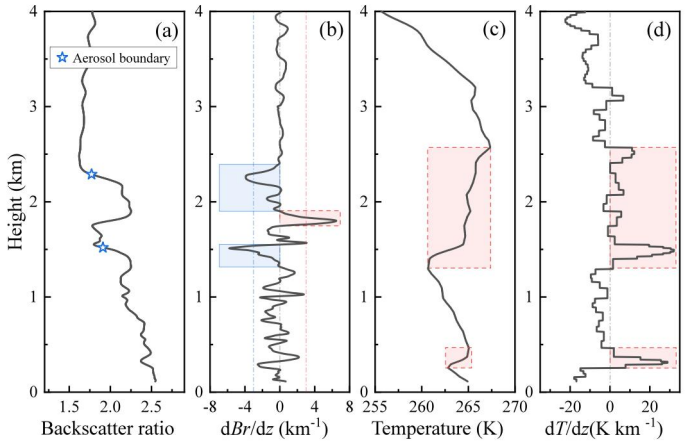

Figure 3. Extraction of UABL and TI characteristics. Panels (a)-(d) show (a) BR, (b) BR gradient, (c) temperature, and (d) temperature gradient. In panels (a)-(d), the black curves represent the BR, BR gradient, temperature, and temperature gradient, respectively. Asterisks indicate the identified aerosol layer boundaries. In panel (b), the blue solid and red dashed shaded regions denote NIBR and PIBR, respectively. In panels (c) and (d), the red dashed shaded regions highlight the TI layers.

Referee comment 5:

Even with the information gathered with the comprehensive set of observations use in this study some statements are a little bit speculative. For example, in line 221, the authors write:" A brief removal of pollutants occurred in the afternoon of 30 December, followed by a rapid re-accumulation during the night.". In fact what you can state is that: "A brief reduction of pollutants occurred in the afternoon of 30 December, followed by a rapid re-accumulation during the night." The origin of the "reduction" could be associated to different causes like the removal, the spreading of these pollutants in a high volume of atmosphere and the advection of these pollutants due to horizontal wind, but the authors do not present evidence for a choice.

Author response:

We thank the reviewer for this insightful comment. We agree that the original wording may imply a specific mechanism for pollutant removal that is not fully supported by the available observations. To avoid potential overinterpretation, we have revised the wording in the manuscript following the reviewer's suggestion. Specifically, the phrase "removal of pollutants" has been replaced with "reduction of pollutants" to provide a more cautious description of the observed change in $PM_{2.5}$ concentration.

The sentence in the manuscript has therefore been revised as follows:

"A brief reduction of pollutants occurred in the afternoon of 30 December, followed by a rapid re-accumulation during the night." (In page 11, lines 245-246)

This modification avoids attributing the reduction to a specific mechanism. In addition, we have carefully reviewed the entire manuscript and revised several statements to ensure that the interpretations remain closely supported by the observations and to avoid potential overinterpretation.

Changes in manuscript:

(1) (In page 21, lines 403-410)

The lidar and radiosonde temperature profiles indicate that a surface-based TI layer with a thickness of up to 600 m developed in the morning of 30 December, effectively suppressing the vertical diffusion of aerosols. Consequently, despite strong north-westerly winds exceeding 8 m s^{-1}

above approximately 1 km during the daytime (Fig. 6h), surface $PM_{2.5}$ concentrations remained persistently high (Fig. 4a). As surface heating intensified, the associated decrease in relative humidity may have promoted aerosol drying and enhanced turbulent mixing in the lower atmosphere, leading to a noticeable reduction in near-surface $PM_{2.5}$ concentrations. However, the duration of surface heating was relatively short, potentially limiting the sustained development of turbulence and thereby restricting efficient vertical transport of aerosols. Later in the day, $PM_{2.5}$ concentrations increased again, possibly associated with aerosol subsidence and hygroscopic growth.

(2) (In page 22, lines 425-429)

The top height of the surface-based TI decreased from approximately 0.7 km at 10:00 to about 0.4 km at 13:00. Meanwhile, the near-surface aerosol backscatter coefficient showed an overall decreasing trend. A pronounced gradient in the backscatter profile corresponded well with the inversion top height. Considering the relatively high near-surface relative humidity (up to 80 %) during this period, the observed decrease in backscatter is likely dominated by aerosol drying in the lower layer, possibly accompanied by moderate aerosol radiative forcing.

Referee comment 6:

In their answers to the Reviewer#1, the authors try to improve the discussion on the stove effect starting in line 305: "... At noon on 24 December, aerosols were primarily concentrated near the surface, potentially favoring the onset of the stove effect. However, the surface-based TI restricted vertical diffusion, resulting in negligible changes in surface $PM_{2.5}$ concentrations." and in this sense they propose the inclusion of a new statement : "However, the warming of the lower layer must overcome the surface inversion formed by nocturnal radiative cooling, which delays the development of near-surface turbulence and may be the primary reason for the relatively modest changes in surface $PM_{2.5}$ concentrations." My concern with this justification is that I can see in the figures a clear effect of surface inversion, that supports this statement. Even with the answer on the overlap effects on temperature offered by the authors, determining the presence of near surface temperature inversion is not easy, having in mind the uncertainties in the temperature profiles in the lower part and the fact that you missed the first 120 m, according to the estimation of the overlap.

Author response:

Thank you for raising this important point. Due to the limitations associated with the overlap correction, reliable temperature retrieval in this study begins at approximately 120 m above the surface. Consequently, the complete structure of the surface-based temperature inversion cannot be fully resolved by the lidar observations. The "near-surface temperature inversion" described in the manuscript therefore refers only to the temperature structure above the reliable retrieval height, rather than the classical surface-based inversion layer.

Although the temperature structure in the lowest layer can be inferred to some extent using radiosonde observations, we have added a clarification at the first occurrence of the term "near-surface inversion" in the manuscript to ensure a more rigorous description:

"It should be noted that the description of the surface-based TI layer here refers only to the region above the reliable temperature retrieval height (>120 m)." (In page 14, lines 312-313)

Regarding the interpretation mentioned in the manuscript, our analysis was also supported by radiosonde temperature profiles. As shown in Fig. 6f (Fig. 5f in the original manuscript), the

radiosonde observation at 07:00 on 24 December indicates the presence of an inversion in the lowest layer. We apologize for not stating this clearly in the previous version. Accordingly, the relevant sentence in the manuscript has been revised as follows:

"However, the radiosonde temperature profile on the morning of 24 December (Fig. 6f) indicates the presence of a near-surface inversion, which may delay surface warming and the development of turbulence in the lower atmosphere and could partly explain the relatively small variation in surface $PM_{2.5}$ concentrations." (In page 18, lines 345-347)

Referee comment 7:

Having in mind the relevance of the stove effect in the discussion of results, does the author measurements of the absorption component of the aerosol, for example with an aethalometer, that can support the development of the stove effect near the surface.

Author response:

We thank the reviewer for this valuable suggestion. Unfortunately, direct measurements of aerosol absorption (e.g., from an aethalometer) were not available in the dataset collected during this experiment. To provide additional supporting evidence, we followed the reviewer's suggestion and calculated the lidar ratio. Since the lidar ratio is influenced by both aerosol scattering and absorption properties, it can provide indirect support for the interpretation of the stove effect near the surface.

We would like to note that this analysis relies on optical properties derived from lidar observations, and direct aerosol absorption measurements were not available for further validation. This limitation has been clarified in the revised manuscript.

Changes in manuscript:

Although direct measurements of aerosol absorption (e.g., from an aethalometer) were not available during this experiment, the lidar ratio can provide indirect information on aerosol optical properties. As shown in Fig. 10d, the increased lidar ratio in the lower layer during the pollution period may suggest enhanced aerosol absorption and support the development of the near-surface stove effect, although this inference has not been directly verified by dedicated absorption measurements. (In page 21, lines 397-401)

Referee comment 8:

In the manuscript the authors mention the extinction coefficient as a product of their measurements, but they do not use this variable. In fact, the lidar ratio that can be derived from the backscatter and extinction profiles could provide confirmation of the absorption component of the aerosol relevant for the development of the dome effect.

Author response:

We thank the reviewer for this constructive suggestion. Following this comment, we further analyzed the extinction coefficient and derived the corresponding lidar ratio at 355 nm ($S = \alpha/\beta$) to better characterize the aerosol optical properties. The updated results are presented in the revised Fig. 10(d), together with the aerosol heating rate shown in Fig. 10(c).

The lidar ratio exhibits a clear vertical variation. In the near-surface layer (below ~300 m), the lidar ratio ranges from approximately 60–80 sr, while at around 1 km altitude it mainly remains within 35–50 sr. According to previous studies, lidar ratios above 60 sr at 355 nm are typically

associated with strongly absorbing urban or pollution aerosols. Therefore, the elevated lidar ratio observed near the surface suggests enhanced aerosol absorption in the lower layer.

Consistent with this feature, the aerosol heating rate (Fig. 10c) also shows pronounced positive values primarily confined to the near-surface layer, indicating stronger radiative heating associated with the accumulation of absorbing aerosols. In contrast, the elevated aerosol layer around 1 km does not show similarly high lidar ratios or heating rates.

These results suggest that the strongest absorption and associated radiative heating are mainly confined to the lower aerosol layer. Consequently, the potential stove effect is more likely related to the accumulation of absorbing aerosols near the surface rather than to an elevated absorbing layer. The manuscript has been revised accordingly to clarify this point.

Changes in manuscript:

(1) (In pages 19-21, lines 367-388)

The hourly evolution of the aerosol vertical structure, atmospheric temperature, and buoyancy acceleration on 25 December is shown in Fig. 10a. Figure 10b presents the variations in temperature tendency, temperature gradient, and TI depth of the elevated TI layer. Figure 10c shows the aerosol heating rate, which is approximately estimated using a simplified shortwave heating formulation in the vertical direction ($Q = 1/(\rho c_p)\cdot dF/dz$), where ρ and c_p denote the air density and the specific heat capacity of air, respectively, and F represents the net radiative flux. The lidar ratio at 355 nm ($S=\alpha/\beta$) is shown in Fig. 10d.

Under the combined influence of the elevated TI and weak surface convection, a dome-like stratified structure began to develop near the UABL. As illustrated in Fig. 10b, after 10:00 local standard time (LST), the temperature tendency around 1.2 km increases significantly and is markedly higher than that in the lower layers, whereas the aerosol heating rate in Fig. 10c remains relatively weak. Backward air-mass trajectory analysis shows that the airflow at approximately 1.5 km is advected from southern regions toward the observation site, indicating a northward transport of warm air. Consequently, horizontal advection may play an important role in the pronounced warming near the upper boundary layer (UABL). Under the combined influence of advective warming and aerosol radiative heating (in Figs. 10c–d), the elevated TI appears to be further intensified. This process is likely to suppress the upward transport of turbulence and induce local aerosol subsidence. Meanwhile, surface warming may enhance buoyancy in the lower atmosphere (in Figs. 10c–d), promoting turbulent uplift of near-surface aerosols. However, the heating rate near the surface remains relatively weak.

As a pronounced stratification develops near the UABL, the heating rate within the aerosol-stratified layer increases substantially, while the warming rate in the lower layer tends to decrease. This reduction may be partly attributed to the attenuation of downward radiative fluxes by the stratified aerosol layer, which could constrain surface warming. Given the mid-latitude location of the study region, the limited duration of daytime solar radiation may have been insufficient to sustain continuous surface heating. Consequently, subsidence within the upper aerosol layer likely became the dominant mechanism regulating vertical aerosol mixing during this period. These interpretations are based on observational consistency and are subject to uncertainties associated with the simplified heating rate estimation.

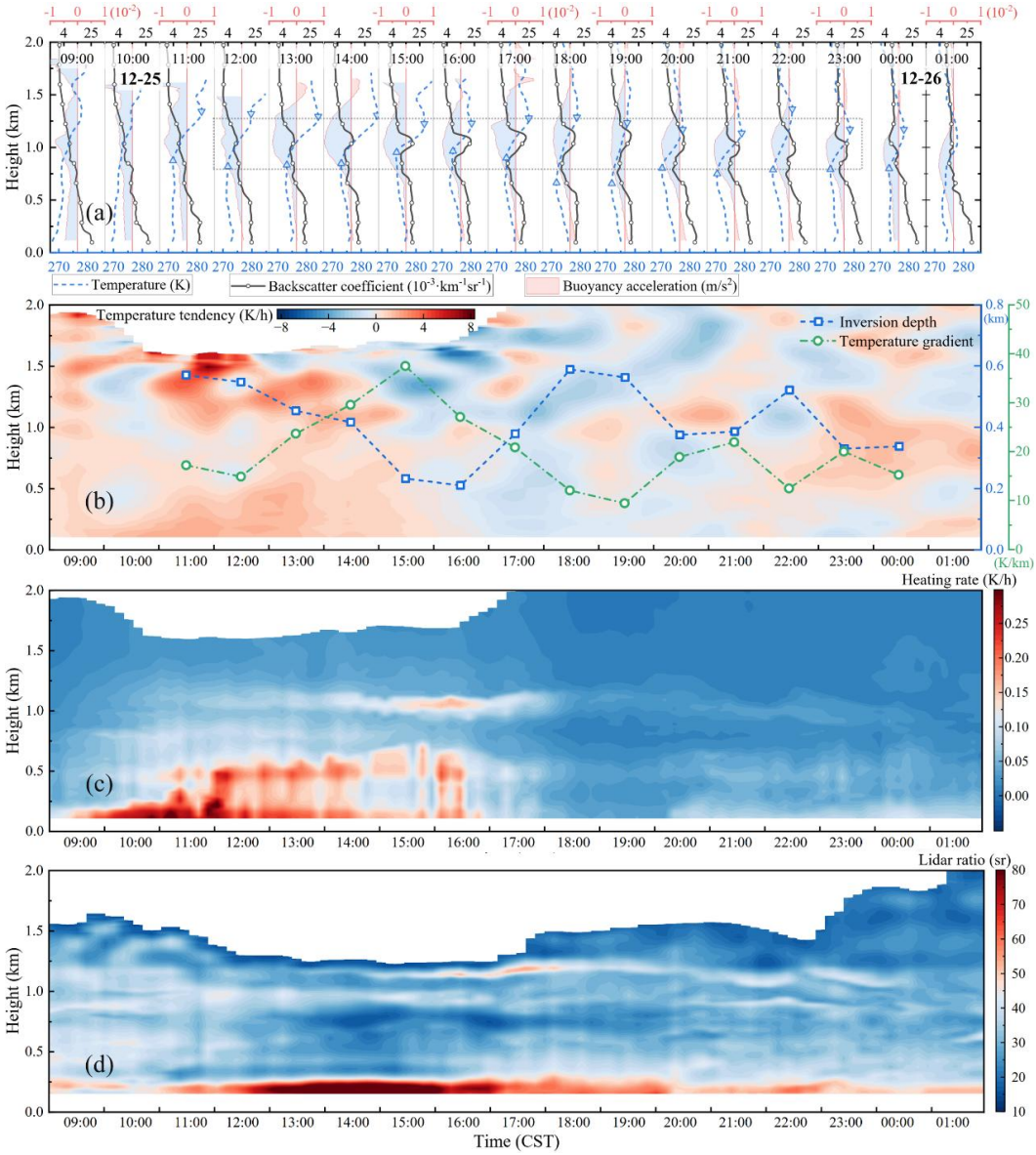

Figure 10. Evolution of the vertical structure and atmospheric buoyancy on 25 December. Panels (a)–(d) show the aerosol and temperature structure, buoyancy acceleration, aerosol heating rate, and lidar ratio (355 nm), respectively. In panel (a), the black line with circle markers represents the aerosol backscatter coefficient, and the blue dashed line denotes the temperature profile. Shading indicates buoyancy acceleration, with blue (red) corresponding to negative (positive) values and downward (upward) buoyant motion. Upward- and downward-pointing triangles indicate the TI layer. In panel (b), the green dotted line shows the temperature gradient, while the blue dash–dotted line with square markers represents the TI depth.

(2) (In page 21, lines 397-401)

Although direct measurements of aerosol absorption (e.g., from an aethalometer) were not available during this experiment, the lidar ratio can provide indirect information on aerosol optical properties. As shown in Fig. 10d, the increased lidar ratio in the lower layer during the pollution period may suggest enhanced aerosol absorption and support the development of the near-surface stove effect, although this inference has not been directly verified by dedicated absorption measurements.

Additional revisions made by the authors:

In addition to the revisions made in response to the referees' comments, we carefully reviewed the

entire manuscript and implemented several additional improvements to enhance the clarity, accuracy, and consistency of the paper. These modifications do not affect the scientific conclusions of the study. The main changes are summarized as follows.

(1) Improvements in wording and clarity

Several statements have been refined to improve readability and scientific rigor. In Fig. 7c, the color bar label has been revised from "*vertical air velocity*" to "vertical velocity" for consistency with standard terminology.

The revised sentences include the following:

- Cloud layers not only suppress radiative heating but may also enhance near-surface humidity through virga processes, which may be conducive to increases in $PM_{2.5}$ concentrations. (In page 1, lines 12-13)
- Comparisons with co-located radiosonde measurements show that the temperature and water vapor uncertainties are within 1 K and 0.5 g kg^{-1}, respectively. (In page 3, lines 82-83)
- The dominant phase of the pollution development stage occurred from 22 to 28 December. Figure 8 shows the vertical distributions of aerosols and temperature during this period, including profiles in the morning and evening, and daily averages. (In page 14, lines 302-303)
- Subsequently, a surface-based TI layer with a thickness of about 1 km developed, strongly inhibiting the vertical diffusion of aerosols. (In page 14, lines 311-312)
- After sunset, a stable layer developed below approximately 1 km, favoring the accumulation of aerosols in the near-surface layer. (In page 17, lines 333-334)
- The pollution dissipation during this episode was incomplete. The dissipation on 2 January 2024 followed a similar mechanism to the first event, but was associated with stronger northwesterly winds. (In page 21, lines 416-417)
- Consequently, the combined effects of radiative heating and strong northwesterly flow resulted in a more complete pollution dissipation during this event. (In page 22, lines 422-423)

(2) Correction of parameter values

Some inaccurately labeled parameters have been corrected. For example, the elastic-scattering suppression ratios listed in Table 1 have been revised to 65, 50, 70, and 70 dB, respectively. (Page 4, Table 1)

(3) Adjustment of figure numbering

After adding the topographic map of the study area, all figure numbers in the manuscript have been updated accordingly to maintain consistency.

(4) Removal of redundant description

A repeated sentence in the original manuscript has been removed:

"During the pollution dissipation stage, enhanced solar radiation restored atmospheric buoyancy and promoted vertical mixing, while horizontal advection facilitated aerosol removal."

(5) Institutional update

Due to an institutional update, the name of the school has been changed from the former School of Mechanical and Precision Instrument Engineering to the School of Optoelectronic Science and Intelligent Instrumentation. This change has been updated throughout the revised manuscript.